



Effect of ultrasonic bonding and lamination on electrical performance of copper indium gallium (di) selenide CIGS thin film photovoltaic solar panel

Hassan Basher^{a†}, Muhammad Nubli Zulkifli^a , Azman Jalar^{b†} and Michael Daenen^{c†}

^aRenewable Energy Research Laboratory (RENERAL), Electrical Engineering Section, British Malaysia Institute, Universiti Kuala Lumpur, Selangor, Malaysia; ^bInstitute of Microengineering and Nanoelectronics (IMEN), Universiti Kebangsaan Malaysia, Selangor, Malaysia; ^cFaculty of Engineering Technology, Hasselt University, Diepenbeek, Belgium

ABSTRACT

This paper aims to study the effect of ultrasonic aluminum (Al) bonding and lamination processes on the electrical performance of copper indium gallium (di)selenide (CIGS) thin film photovoltaic (TFPV) solar panels. Ultrasonic Al bonding on the MoSe₂ layer of the CIGS TFPV solar panel was performed in three configurations: eight bonds, 16 bonds, and parallel configurations. The lamination process was performed on the Al bonds with MoSe₂ layers of the CIGS TFPV solar panel. Ultrasonic bonding and lamination processes significantly affect the electrical performance of CIGS TFPV solar panels. Open circuit voltage, V_{oc} is the least affected electrical characteristic with the application of ultrasonic bonding and lamination processes as compared to short circuit current (I_{sc}), current density (J_{sc}), maximum power (P_{mpp}), fill factor (FF), and efficiency. 8-bonds configuration has the highest efficiency, ranging from 11.45% to 13.86% throughout unique connections of I-V measurement, compared to 16-bonds ranging from 7.99% to 10.77%, and parallel configurations, ranging from 9.14% to 11.92%. The notable variations in electrical properties with the processes used to create laminated CIGS TFPV solar panels with ultrasonic Al bonding can be explained by physical examination and lock-in infrared (IR) thermography. The ultrasonic Al bond is best suited to be used as the interconnection mean in the CIGS TFPV solar panel compared to that of conductive adhesive that has been widely applied nowadays.

ARTICLE HISTORY

Received 21 May 2023
Revised 8 December 2023
Accepted 20 December 2023

KEYWORDS

CIGS solar panel;
ultrasonic Al bond;
lamination; I-V
measurement; IR
thermography; Mo back
contact

1. Introduction

The solar panel manufacturer has recently applied ultrasonic Aluminum (Al) bonding as the interconnection technology because of less creation of high temperature,

CONTACT Muhammad Nubli Zulkifli  mnubliz@unikl.edu.my.

[†]Co-author authors.

© 2024 Informa UK Limited, trading as Taylor & Francis Group

solid-state type of adhesion, room temperature operation, and cost-effectiveness [1, 2]. However, the detailed analysis of the effect of applying ultrasonic bonding on the performance of CIGS TFPV solar panels still requires further study. It is because every step taken to connect the dissimilar metals of Al ribbon onto Mo back contact layer using ultrasonic bonding will affect the performance of the CIGS TFPV solar panel. Ultrasonic bonding of dissimilar metals is made by applying different parameter windows of bonding parameters, namely bonding pressure, bonding energy, and bonding amplitude, to name a few. These bonding parameters directly affect the bondability and mechanical and electrical performances of the CIGS TFPV solar panel. Several studies were performed to evaluate the effect of ultrasonic bonding parameters on the bondability and mechanical and electrical performances of dissimilar metal bonds. Ding et al. [3] conducted the finite element analysis or numerical study to simulate the deformation in ultrasonic bonding. They reported that the bonding force of pressure and bonding power or energy plays a significant role in changing the contact pressure and frictional energy intensity. Zhang et al. [4] conducted a microstructure study to investigate the Al ribbon weldability or bondability. They reported that the joint formation process comprises several steps for different bonding time duration with the combination of fracture, creation of thin alloy, detachment, and series of slipping. Jing et al. [5] reported that the bond resistance was changed between $64.5\text{ m}\Omega$ to $72.5\text{ m}\Omega$ with increased bonding power or energy value. They inferred this is because of the changes in interfacial joining area, bond wire deformation, and internal defects.

The manufacturer critically needs the relationship between the electrical performance and defects created during the manufacturing process of a photovoltaic solar panel to produce high-quality, reliable, and cost-effective solar panels. Visual inspection, infrared (IR) thermography and current-voltage (I-V) curve measurement are some of the characterization methods used to evaluate the performance of PV solar panels. Several studies have shown that the combined evaluation using visual inspection, IR thermography, and I-V measurement would produce a comprehensive analysis of solar panels. Tsanakas et al. [6] reviewed the classification of dominant fault, degradation modes, and fault diagnosis using outdoor IR imaging of silicon photovoltaic solar modules. They concluded that specific thermal signatures and I-V characteristics could be assigned to at least one fault and degradation mode. Wehrmann et al. [7] performed the dark lock-in IR thermography (DLIT) and morphology inspection using an optical microscope and scanning electron microscope (SEM) on the laser scribing or patterning of the CIGS TFPV solar panel. They found a correlation between the DLIT, SEM, and optical images to identify the shunt defect formation due to the laser scribing. Misic et al. [8] performed electroluminescence (EL) and dark lock-in thermography (DLIT) to study the defects created due to laser scribing (P1) and mechanical scribing (P2, P3) of CIGS TFPV solar panel. They reported that the EL images do not allow a non-ambiguous defect distinction, while DLIT can reveal defect patterns. They also suggested that image processing software can use the DLIT defect patterns for the defect diagnostic application. Thus, the combined evaluation using different characterization methods could help to determine the failure mechanisms and consequently the overall performance of TFPV solar panel.

To make a good solar panel, the flaws that appear during production still need to be fully studied using a variety of different characterization methods. This is especially true for the ultrasonic Al bonding process of CIGS TFPV solar panels. In the present study, ultrasonic bonding was used to connect the Al ribbon onto the thin layer of MoSe_2 on top of the Mo back-contact layer of the CIGS TFPV solar panel. The MoSe_2 layer was thinned without damaging Mo back-contact layer using mechanical brushing and scribing methods. Three ultrasonic Al bonds or sample configurations were made on the CIGS TFPV solar panel: 8-bonds, 16-bonds, and a parallel connection of two CIGS TPFV solar panel configurations. The current-voltage (I-V) and power-voltage (P-V) curves measurements were carried out on every three selected configurations based on four connections, namely before bonding, after bonding, after bonding (on the busbar), and after lamination connections. The physical observation was performed by inspecting the physical changes in the created ultrasonic Al bonds and the overall appearance of the CIGS TFPV solar panel. Lock-in infra-red (IR) thermography was performed on every three selected configurations to determine the location of defects by identifying hot spots.

2. Materials and methods

Using a mechanical brushing tool followed by a mechanical scribe, the layers of the CIGS TFPV solar panel were removed up to the thin layer of MoSe_2 , much like in a preliminary investigation [9]. According to a preliminary investigation [9], mechanical brushing and scribing operations left a thin layer of MoSe_2 with an average thickness of 5.3 nm on top of the Mo back contact layer. Figure 1 demonstrates the diagram of CIGS TFPV solar panel construction used for the current study. The construction of each layer involves several processes, namely, metal

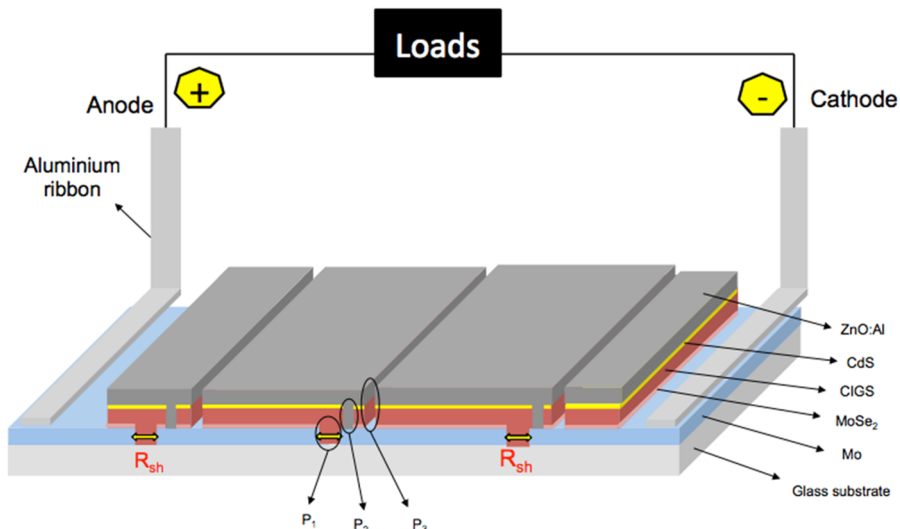


Figure 1. Diagram of CIGS TFPV solar panel with two-finished conducting strips monolithically integrated using ultrasonic Al bonding [10].

sputtering, laser patterning (P1, P2, and P3), metal evaporation, chemical bath deposition, mechanical scribing, and lamination or encapsulation [10]

Once the CIGS layers had been removed and a thin coating of MoSe_2 was present, ultrasonic bonding was carried out. The CIGS TFPV solar panel's thin layer of MoSe_2 on top of the Mo back-contact layer was bonded using an ultrasonic bonder, the Schunk DS-35, and aluminium ribbon with dimensions of 0.15 mm in thickness and 2 mm in width. Al bonds and conductive adhesives were used to create two-finned conducting strips monolithically integrated interconnection on CIGS TFPV solar panel as shown in Figure 1.

The ultrasonic bonder uses a sonotrode (welder's head) that is $5 \times 3 \text{ mm}^2$ in size. The ribbon, direction of applied bonding pressure, and amplitude are shown in Figure 2 together with a cross-sectional schematic depiction of an ultrasonic Al bond.

To determine the optimal bonding settings and prevent the development of bonding failure modes including substrate fracture, non-stick bonds, and broken ribbons, to mention a few, a preliminary investigation was conducted [11]. The parameter window for the bonding parameters, bonding pressure, bonding maximum energy, and bonding amplitude, which were determined from the preliminary study for the construction of 8-bonds and 16-bonds configurations, respectively, is shown in Table 1 [11]. The distance between each bond was set to be 1.2 cm and 0.6 cm, respectively, to create the 8-bonds and 16-bonds configurations. The dimension of the CIGS TFPV solar panel used for the current study is $(14.6 \times 14.8) \text{ cm}^2$. 8-bonds and 16-bonds configurations were chosen to compare the two extremes' bonds from the lower to the higher number of bonds that could be created on the solar panel of $(14.6 \times 14.8) \text{ cm}^2$.

Three ultrasonic Al bonds or sample configurations were made on the CIGS TFPV solar panel: 8-bonds, 16-bonds, and parallel configurations. A parallel configuration was constructed by connecting two CIGS TPFV solar panels using a parallel connection, with each solar panel having eight bonds of ultrasonic Al bonds.

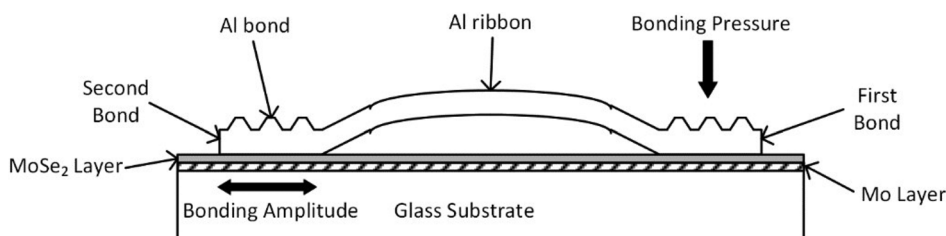


Figure 2. Cross-sectional schematic view of ultrasonic Al bond and ribbon. Black arrows show the direction of bonding pressure and amplitude [9].

Table 1. Ultrasonic bonding parameter window.

Bonding parameter	Value
Pressure (bar)	3
Maximum Energy (Ws)	20
Amplitude (μm)	7.7

Al bonds with Mo and MoSe₂ layers were laminated using an Arkama R999A ethylene vinyl acetate (EVA) encapsulant, following the procedure from the preliminary work [9]. A laminator machine was utilised to perform the lamination procedure, which involved heating the sandwich of glass, polymer sheet, the active surface of CIGS TFPV with Al bonds, and the glass substrate to 158 °C and applying clamp pressure of 1 bar for 16 min.

Crocodile clips were connected under four different conditions: before bonding, after bonding (on the busbar), and after lamination. Current-voltage (I-V) and power-voltage (P-V) curve measurements were made for each of the three configurations that were chosen. Under the illumination of an Atlas Solar Constant 1200 lamp, at a temperature of 25 °C, and with a relative humidity (RH) of 30%, measurements of the current-voltage (I-V) and power-voltage (P-V) curves were made. From the measurement of the I-V and P-V curves, other electrical properties like open circuit voltage (V_{oc}), short circuit current (I_{sc}), current density (J_{sc}), maximum power (P_{mpp}), fill factor (FF), and efficiency were also obtained. Figure 3 depicts the experimental setup for the placement of crocodile clips for the curve tracer of I-V measurement at various bonding stages, including before bonding, after bonding (on the busbar), and after laminations connections. To ascertain the changes in electrical performance with the actions made for packaging the CIGS TFPV solar panel, the curve tracer was connected at a different site, as illustrated in Figure 3. Physical changes in the newly produced ultrasonic Al bonds and the general look of the CIGS TFPV solar panel were examined as part of the physical observation.

Lock-in infrared (IR) thermography was carried out to identify the hot spot location generated because of the deformation during the ultrasonic bonding and lamination process of the CIGS TFPV solar panel. Lock-in IR thermography is one of the non-destructive tests that can be performed with no sample preparation [12]. For the current study, the lock-in IR thermography test was conducted on the encapsulated CIGS TFPV solar panel with three configurations of ultrasonic Al bonds. Lock-in IR thermography is a method to convert IR radiation or IR energy into a thermograph without making any physical contact with the sample under test. This method can evaluate the subsurface characteristics of materials [13]. Figure 4 illustrates the schematic of the experimental setup for the

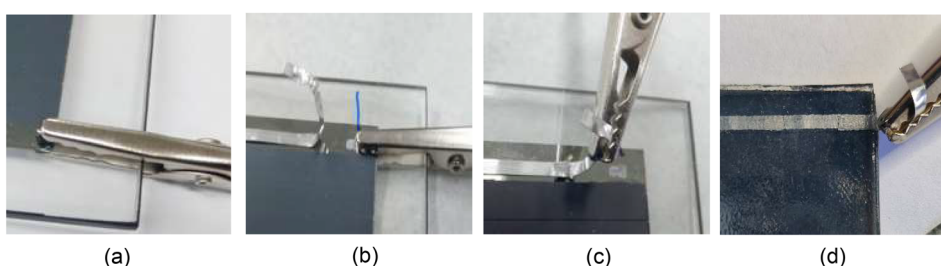


Figure 3. Location of crocodile clips for the I-V measurement, namely a) before bonding, b) after bonding, c) after bonding (on the busbar), and d) after lamination.

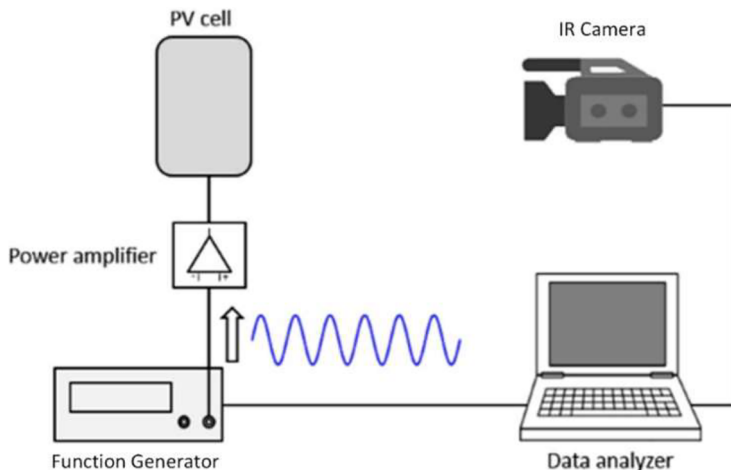


Figure 4. Schematic of the experimental setup for IR thermography on encapsulated CIGS TFPV solar panel.

non-destructive lock-in IR thermography test performed on the encapsulated CIGS TFPV solar panel.

The lock-in IR thermography was operated based on the excitation of a periodic thermal signal generated on the device under test or for the current study CIGS TFPV solar panel [14]. The periodic thermal signal generated from the waveform or function generator, as shown in Figure 3, is based on the Joule heating phenomenon [15]. For the current study, the function generator generated a sinusoidal voltage of 1 Hz, ranging from 0.8 V and 5 V. This sinusoidal signal was amplified with an amplification factor of 6.6 using a power amplifier that produced a sinusoidal current ranging from 0.25 A to 1 A. IR camera then observed the changes in IR images on the CIGS TFPV solar panel for a specific time, frame rate, and resolution. The IR images obtained from the lock-in IR thermography were from darker or black to brighter or white, with the darker image representing the hot spot. Hot-spot identification is beneficial to determine the location of subsurface defects in the non-destructive manner that may be created due to the induced stress from the fabrication process of the CIGS TFPV solar panel, including the ultrasonic bonding and lamination processes.

Besides that, of laminated CIGS TFPV, solar panels with ultrasonic Al bonding, I-V, and P-V measurements on laminated CIGS TFPV solar panels with conductive adhesive of copper tape have been carried out. This measurement was taken to evaluate the widely used interconnection technology of conductive adhesive with the current study of the application of ultrasonic Al bonding on CIGS TFPV solar panels.

3. Results and discussion

Figure 5(a–c) depict the current-voltage (I-V) curves obtained from the I-V measurement using a curve tracer under the irradiation of Atlas Solar Constant 1200

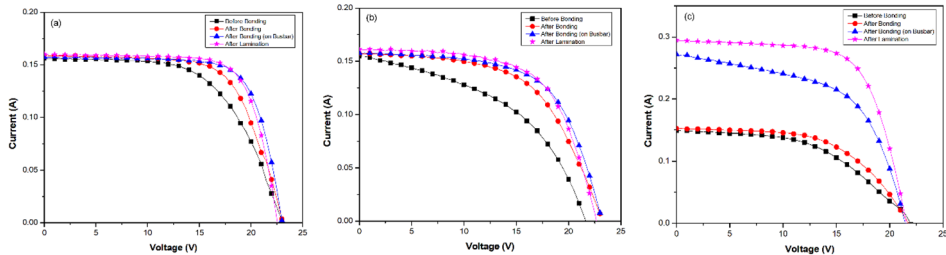


Figure 5. I-V curves of (a) 8-bonds, (b) 16-bonds, and (c) parallel configurations.

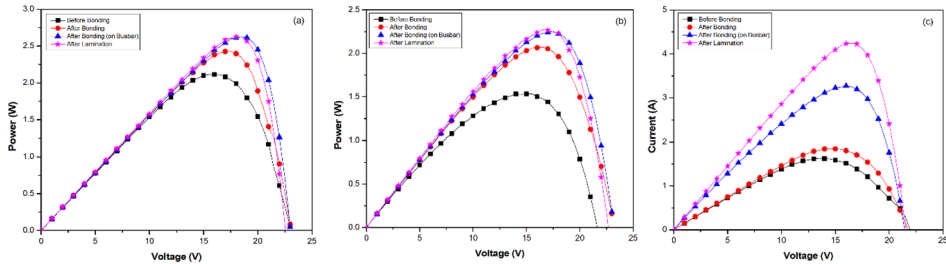


Figure 6. P-V curves of (a) 8-bonds, (b) 16-bonds and (c) parallel configurations.

lamp for 8-bonds, 16-bonds, and parallel configurations, respectively. Figure 6(a–c) show the power-voltage (P-V) curves obtained from the I-V measurement for 8-bonds, 16-bonds, and parallel configurations, respectively. Figures 5 and 6 show that each curve has different shape variations and minimum and maximum current, voltage, and power values. To further analyze the changes of each parameter that can be derived from the I-V and P-V curves of Figures 5 and 6, respectively, the variation of derived parameters, namely open circuit voltage (V_{oc}), short circuit current (I_{sc}), current density (J_{sc}), output power (P_{mpp}), fill factor (FF), and efficiency towards ultrasonic Al bond configurations are illustrated on Figures 7–12, respectively.

Several studies reported that the variation in each electrical characteristic signifies the occurrence of defects or failure modes in photovoltaic solar panels [6, 16–18]. Figures 7–12 show that the variation for each electrical characteristic between the connections of I-V measurement and ultrasonic Al bond configurations have different trends. In Figure 7, it is noted that V_{oc} is decreasing with the connections of I-V measurement. In addition, the standard error variation of V_{oc} towards ultrasonic Al bond configurations is relatively slight, ranging from 0.47% to 1.42% as compared to that of I_{sc} , J_{sc} , P_{mpp} , FF, and efficiency ranging from 0.66% to 17.77%, 0.49% to 2.46%, 4.95% to 22.48%, 4.81% to 6.75%, and 4.95% to 8.43%, respectively. Several studies indicated that the reduction of V_{oc} followed by the reduction of FF, P_{mpp} , and efficiency indicate the defects occurrence of potential induced degradation (PID) and internal short circuit [6]. The FF, P_{mpp} , and efficiency have an increasing trend with the connections of I-V measurement even though the V_{oc} is reduced. Furthermore, no reliability test was conducted on the CIGS TFPV solar panel to create the PID. Therefore, V_{oc} is the least affected electrical characteristic with the changes of connection of I-V measurement for each ultrasonic Al bonds configuration.

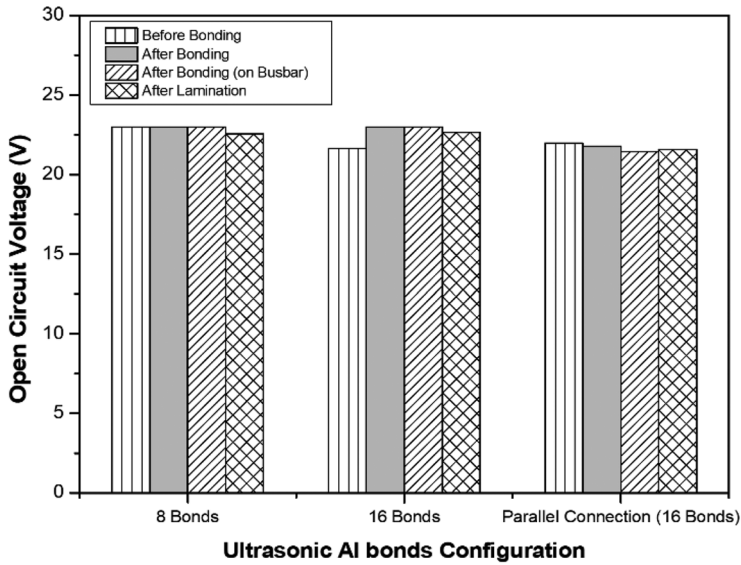


Figure 7. Variation of open circuit voltage, V_{oc} towards ultrasonic Al bonds configuration.

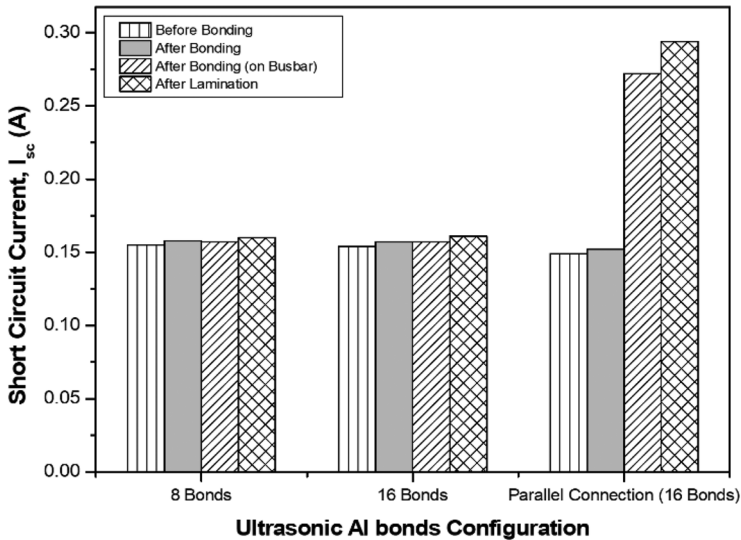


Figure 8. Variation of short circuit current, I_{sc} towards ultrasonic Al bond configurations.

From [Figure 7](#), V_{oc} changes for 8-bonds configuration have the most negligible variation with a standard error of 0.47% compared to 16-bonds and parallel connection configurations with standard errors of 1.41% and 0.52%, respectively. Both bonding (on the busbar) and lamination connections greatly lower the V_{oc} values. The trend of the I_{sc} , J_{sc} , P_{mpp} , FF, and efficiency towards 8-bonds design is also increasing with the connections of I-V measurement, as illustrated in [Figures 8–12](#). The 8-bonds arrangement was made using a CIGS TFPV solar panel, and this trend demonstrates several minor flaws in the solar panel. The CIGS TFPV solar panel's

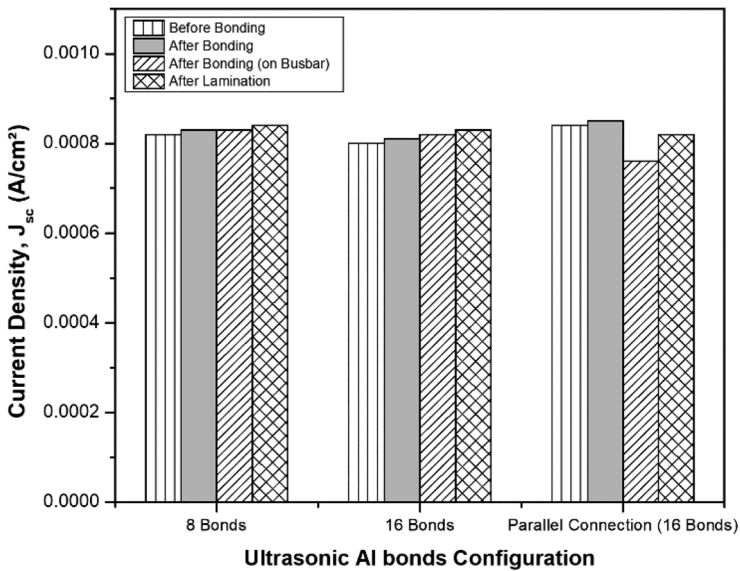


Figure 9. Variation of current density, J_{sc} towards ultrasonic Al bond configurations.

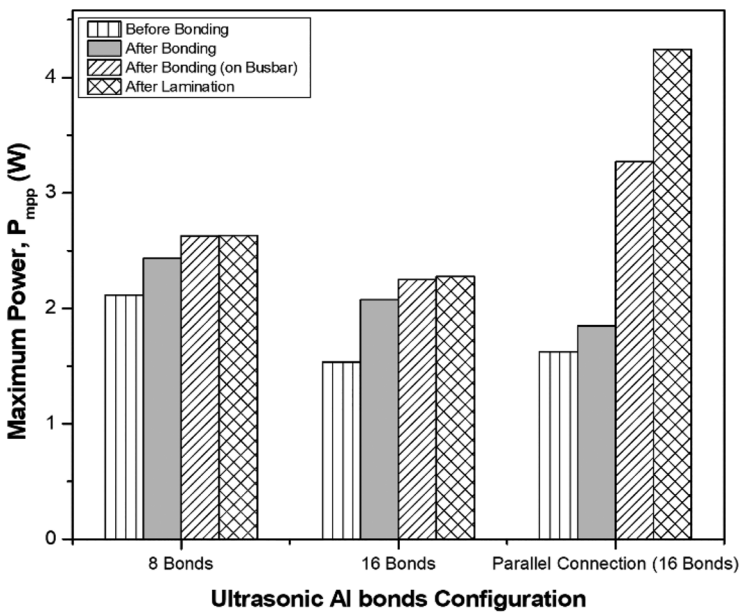


Figure 10. Variation of maximum power, P_{mpp} towards ultrasonic Al bond configurations.

efficiency has increased thanks to the subsequent lamination and ultrasonic bonding operations [16]. According to a preliminary investigation, increasing the cumulative contact area between Al bonds and ribbon by applying optimised parameter windows for ultrasonic Al bonding with bonds spaced 1.2 cm apart has reduced the contact resistance, R_c [11]. The cumulative contact area value was influenced by two different types of connections: the Al bond microweld and the barely touching Al ribbon

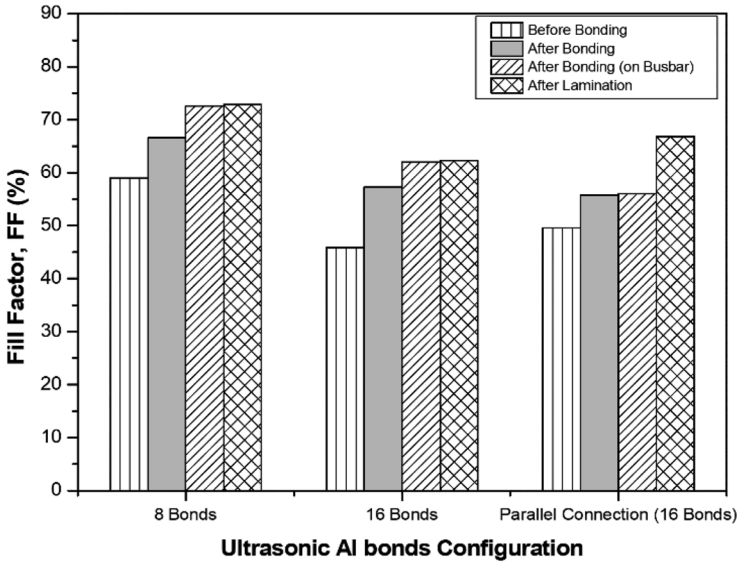


Figure 11. Variation fill factor, FF towards ultrasonic Al bond configurations.

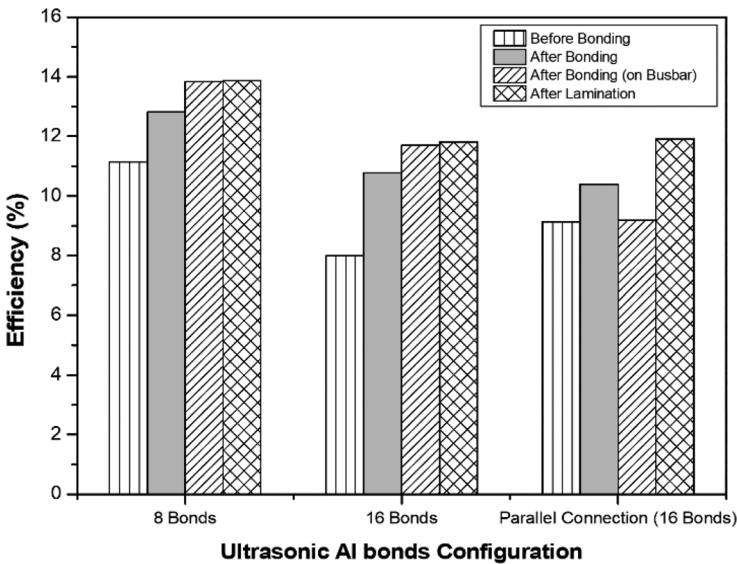


Figure 12. Variation of efficiency towards ultrasonic Al bond configurations.

with Mo rear contact layer. It is well known that efficiency and R_c have an inverse relationship. Therefore, the reduction in R_c or the increase in the cumulative contact area between ultrasonic Al bonds and ribbon with a Mo back contact layer is what causes the rise in efficiency in the case of an 8-bond arrangement from before bonding until after bonding (on the busbar) connections [19].

Figures 10–12 also depict a slight improvement in P_{mpp} , FF, and efficiency for an 8-bond configuration after bonding (on the busbar) and after lamination

connections. This tiny increment occurred because there was just enough space for the Al ribbon and Mo to touch each other, barely expanding the total contact area. The combined effects of thermal expansion owing to temperature ramping, contraction due to curing, and clamping force during lamination have further restricted the ductility of Al ribbon, preventing it from penetrating further down MoSe_2 to barely touch Mo back contact layer [20]. However, the cumulative contact resistance is still increasing with the small amount of improvement as opposed to that of ultrasonic Al bonding on pure Mo back contact layer that has an adverse effect of reducing contact resistance. It is due to different reactions during the lamination process, as mentioned in the preliminary study [11]. Hence, the highest efficiency value for 8-bonds configuration throughout different connections of I-V measurement compared to that of 16-bonds and parallel configurations is due to the higher cumulative contact area of ultrasonic Al bonds and ribbons.

Figure 7 shows that changes of V_{oc} for the case of 16-bonds configuration are different with 8-bonds and parallel configuration. The changes of V_{oc} start with the lower value before bonding connection and then increase after bonding connection, followed by gradually decreasing until after lamination connection. V_{oc} is directly proportionate with R_{sh} and thus significantly affects the FF, P_{mpp} , and efficiency to have the lowest values compared to that of 8-bonds and parallel connections, as seen for the case of 16-bonds configuration before bonding connection in Figures 10–12, respectively [6]. The reduction of R_{sh} that lead to the reduction of FF, P_{mpp} , and efficiency is due to the short-circuited or shunted cells created by the mechanical loading prior to the application of ultrasonic bonding [21]. For the case of 16-bonds configuration, the lower value of V_{oc} , R_{sh} , FF, V_{mpp} , and efficiency happened before bonding connection. This means that the short-circuited and shunted cell defects were created before the ultrasonic Al bonding and lamination processes took place. The subsequent steps after bonding (on the busbar) and after lamination connections have increased the I_{sc} , J_{sc} , V_{mpp} , FF, and efficiency of the 16-bonds configuration. This increment shows that the application of ultrasonic bonding and lamination process has increased the quality of the electron flows leading to the increment in efficiency. Like that of 8-bonds configuration, it is shown that the application of ultrasonic bonding and lamination process has decreased the R_c or increased the efficiency. It is due to the increment of cumulative contact area between ultrasonic Al bonds and ribbon with Mo back contact layer of CIGS TFPV solar panel. Thus, it is noted that the unique variation of electrical characteristics of the 16-bonds configuration compared to that of the 8-bonds and parallel connection configuration is due to the possession of defects, namely short-circuited and shunted cells prior to the ultrasonic bonding. Further, the lowest efficiency value for 16-bonds configuration, particularly after the lamination process, as compared to that of 8-bonds and parallel connection configurations, is due to the minor cumulative contact area created between ultrasonic Al bonds and ribbon with Mo back contact layer.

For the case of parallel configuration, the changes of V_{oc} , I_{sc} , J_{sc} , P_{mpp} , FF, and efficiency are almost like that of 8 bonds but with some differences, especially between after bonding (on the busbar) and after lamination connections. The parallel configuration of two CIGS TFPV solar panels increases the current value [22,23]. Therefore, the I_{sc} increases significantly between after bonding and after bonding

(on the busbar) connections. It is because after bonding connection only measures the electrical performance of one CIGS TFPV solar panel rather than after bonding (on the busbar) connection that measures two CIGS TFPV solar panels with parallel configuration. The I_{sc} is almost double from 0.15 A to 0.27 A for after bonding and after bonding (on the busbar) connections, respectively.

Similarly, P_{mpp} is also increasing, particularly between after bonding and after bonding (on the busbar) connections like I_{sc} . However, the efficiency of parallel connection has a different variation compared to that of I_{sc} , P_{mpp} , and FF. The efficiency increases before and after bonding connections and decreases between after bonding and after bonding (on the busbar) connections. Finally, increasing again after bonding (on the busbar) and after lamination connections, as shown in Figure 12. Similarly, there are minor or almost no significant changes in FF between after bonding and after bonding (on the busbar) connections with values of 55.76% and 56.05%, respectively, before abruptly increasing between after bonding (on the busbar) and after lamination connections as exhibited in Figure 11. The small changes of FF indicate that the recombination process is not occurring in a complete flow due to the leakages between ultrasonic Al bonds and Mo back contact layer [24,25]. It is because a wide gap exists between two CIGS TFPV solar panels at the edges of the panel. Even though the cumulative I_{sc} and P_{mpp} are high, the current or power leakage highly occurred between the Al ribbon and Mo back contact layer of the CIGS TFPV solar panel, especially during the I-V measurement after bonding (on the busbar) connection. The current leakage phenomenon could be identified through the sudden decrement of J_{sc} between after bonding and after bonding (on the busbar) connections with the reduction of value of 0.00085 A/cm² to 0.00076 A/cm², respectively. Several studies have indicated that the reduction of J_{sc} represents the decrement of the current flow or leakage that might happen around the edges of solar panels or between contact of different polarities [26,27]. Therefore, short increments of I_{sc} and P_{mpp} and sudden decrement of J_{sc} and efficiency for the parallel configuration between after bonding and after bonding (on the busbar) connections are due to a gap along the edges of two CIGS TFPV solar panels. It has increased the possibility of current leakages happening prior to the lamination process.

The application of the lamination process that took place after ultrasonic bonding has filled in the gap between the edges of two CIGS TFPV solar panels used for parallel configuration. As mentioned earlier, a couple of forces, namely thermal expansion, contraction, and clamping force, were applied during the lamination process that led to the increment of cumulative contact area between ultrasonic Al bonds and ribbon with Mo back contact layer of CIGS TFPV solar panel. The differences in coefficient of thermal expansion (CTE) and the sizeable gap between CIGS TFPV solar panel has increased the possibility of Al ribbon expanding further into the Mo back contact layer [28,29]. It is due to the expansion of metals, namely Mo back contact and Al ribbon, which would further increase, especially at the periphery or the gap between two CIGS TFPV solar panels, as indicated in Figure 13(c). The thermal expansion created during the lamination process, particularly the temperature ramping duration up until 158 °C, will force metals like Mo back contact layer and Al ribbon to expand further at the gap area between the solar panel and hence could directly touch with each other.

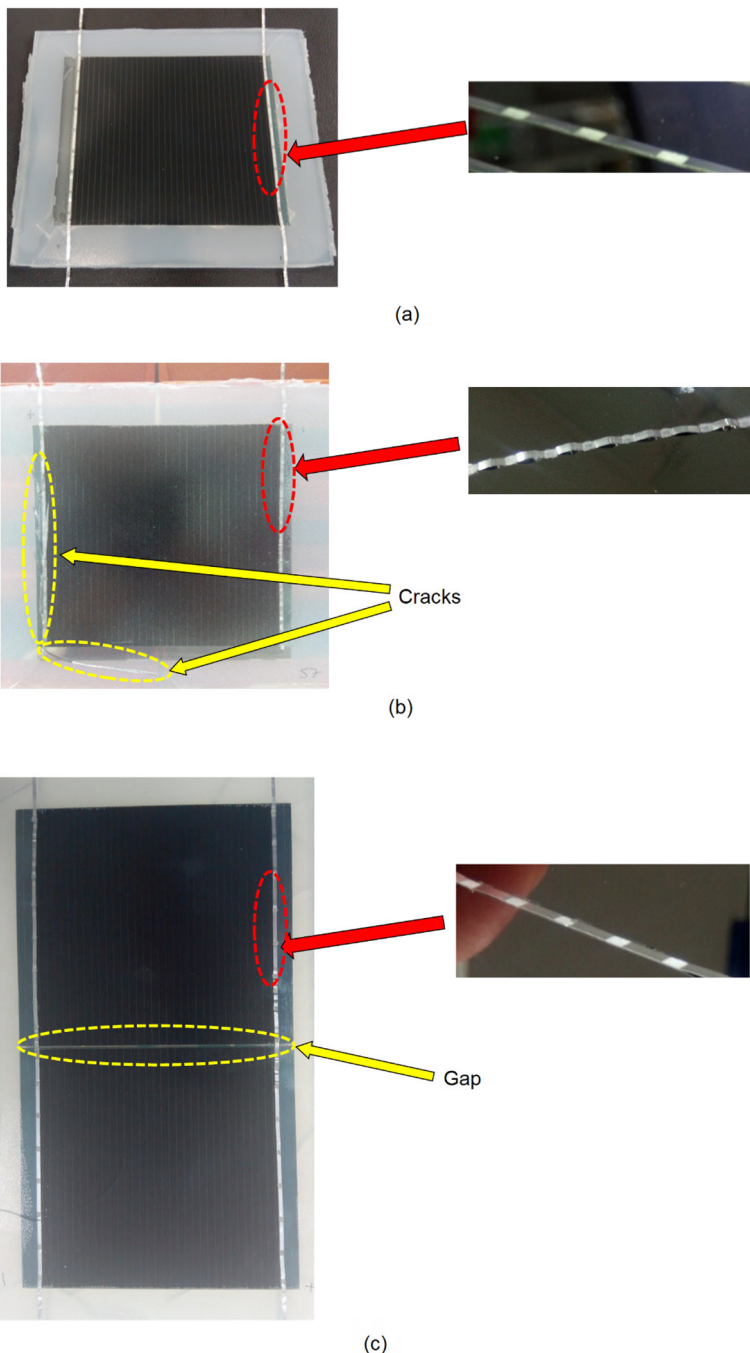


Figure 13. Top view of CIGS TFPV solar panels with (a) 8-bonds, (b) 16-bonds, and (c) parallel configurations.

Furthermore, the clamping force provided during the lamination process will flatten the Al ribbon to penetrate further down MoSe₂ and can barely touch Mo back contact layer [30]. Once the curing period occurs during the lamination

process, the encapsulant used as the lamination material is cured due to cross-linking phenomenon and lets the barely touching Al ribbon and Mo back contact layer remain connected [31]. It could significantly increase the cumulative contact area between the Al bond and ribbon with Mo back contact layer for the parallel connection configuration. Further, the value of J_{sc} increased quite abruptly from 0.00076 A/cm^2 to 0.00082 A/cm^2 for after bonding (on the busbar) and after lamination connections, respectively. Thus, the increment of cumulative contact area that led to the increase of efficiency of parallel configuration is due to the combined effects of thermal expansion, curing, and clamping forces that occurred during the lamination process.

[Figures 13\(a–c\)](#) illustrate the top view of the CIGS TFPV solar panel with 8-bonds, 16-bonds, and parallel connection configurations, respectively. In this figure, the inset at the top right side shows the shape of ultrasonic Al bonds and ribbon at the dotted red lines area. [Figure 13\(a\)](#) shows that 8-bonds configuration has the ultrasonic Al bonds and ribbon with a uniform and straight shape. From the preliminary study, uniform ultrasonic Al bond and ribbon with a straight shape have the highest peel strength and lowest R_c because of higher micro weld creation [11]. It has been proved through the quantitative (R_c and peel strength) and qualitative (load-distance profile) results.

In contrast, 16 bonds configuration have nonuniform ultrasonic Al bonds and a wavy ribbon shape, as shown in [Figure 13\(b\)](#). It is due to the application of a lower distance of 0.6 cm between each bond that could not provide enough elasticity for the ultrasonic Al bonds to have an appropriate departure and arrival of touchdown of sonotrode onto the MoSe_2 layer. Consequently, the bonds created are less adhesive due to the lack of creation of micro weld between Al bond and Mo back contact layer, which increases the R_c and subsequently decreases the efficiency. Furthermore, [Figure 13\(b\)](#) shows that cracks (dotted yellow lines) are located on top of the ultrasonic Al bonds and propagate to the edge of the CIGS TFPV solar panel that has gone through the lamination process. The nonuniform and wavy shape of ultrasonic Al bonds and ribbons might induce the critical stress point that has created cracks [32]. It could be one of the reasons why the V_{oc} is decreased and P_{mpp} , FF, and efficiency are varied in the slightest changes after bonding (on the busbar) and after lamination connections of 16-bonds configuration [16]. Whereas, for the case of parallel connection configuration, significant changes in electrical characteristics, especially I_{sc} , J_{sc} , P_{mpp} , FF, and efficiency, occurred after bonding (on the busbar) and after lamination connections. A wide gap between the two edges of the CIGS TFPV solar panel, as shown in [Figure 13\(c\)](#), could be the main reason for the significant changes in electrical characteristics after bonding and after lamination connections for parallel connection configuration. Thus, physical inspection in terms of the shape of the ultrasonic bonds and ribbon, location of gap, and the occurrence of cracks on the glass substrate can be used to explain the significant changes in electrical characteristics with the steps taken to produce laminated CIGS TPFV solar panel with the ultrasonic Al bonds.

Besides physical inspection, the lock-in IR thermography analysis has also been performed to identify the defects that might affect the electrical performance of the CIGS TFPV solar panel with ultrasonic Al bonding. It is because the lock-in IR

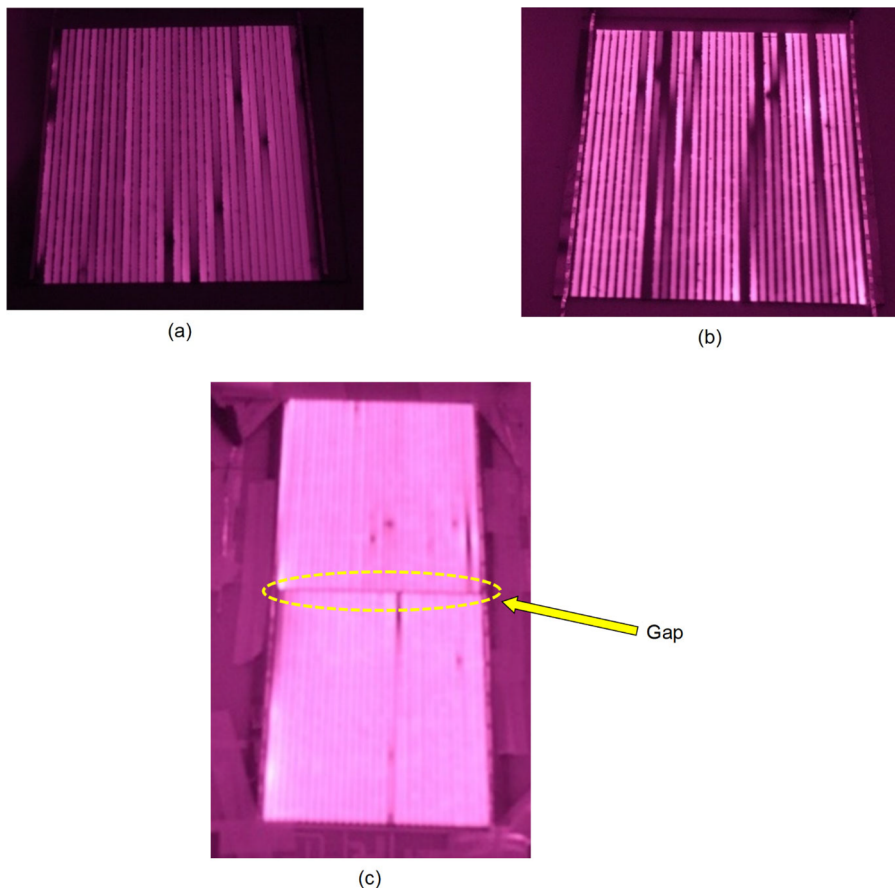


Figure 14. Lock-in IR thermography images for (a) 8-bonds, (b) 16-bonds, (c) parallel configurations.

thermography image can identify the subsurface defect that existed in the photovoltaic solar panels [13]. Figure 14 shows that each of the CIGS TFPV solar panels has a different distribution of dark and bright areas. It is noted that CIGS TFPV solar panel with 16-bonds configuration has a darker area than 8-bonds and parallel configurations. In addition, it is shown that the dark area of the 16-bonds configuration is located mainly around the area of the active cells compared to that of 8 bonds and parallel configurations of CGIS TFPV solar panels.

Furthermore, sub-surface defects created after ultrasonic bonding application can also be identified through the higher alternating darker and brighter areas of lock-in IR image at the Al bonds and ribbon the busbar of 16-bonds configuration of CIGS TFPV solar panel. These observations further confirm the early finding that the lower value of V_{oc} before bonding connection of 16-bonds configuration could be due to the short-circuited and shunted cell. Besides, this observation also might explain the inconsistent bonding pressure applied on the CIGS TFPV solar panel that can be seen through the nonuniform shape of ultrasonic All bonds and ribbons. Consequently, this has reduced the overall efficiency of 16-bonds

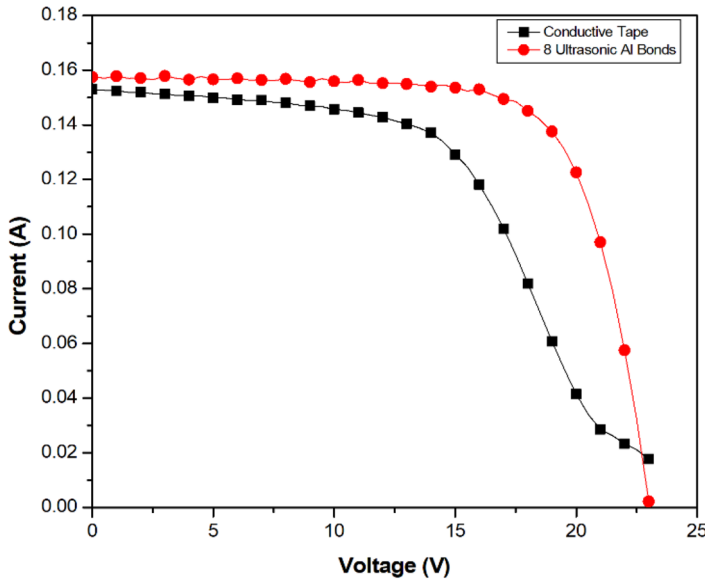


Figure 15. I-V curves of 8-bonds and conductive adhesive.

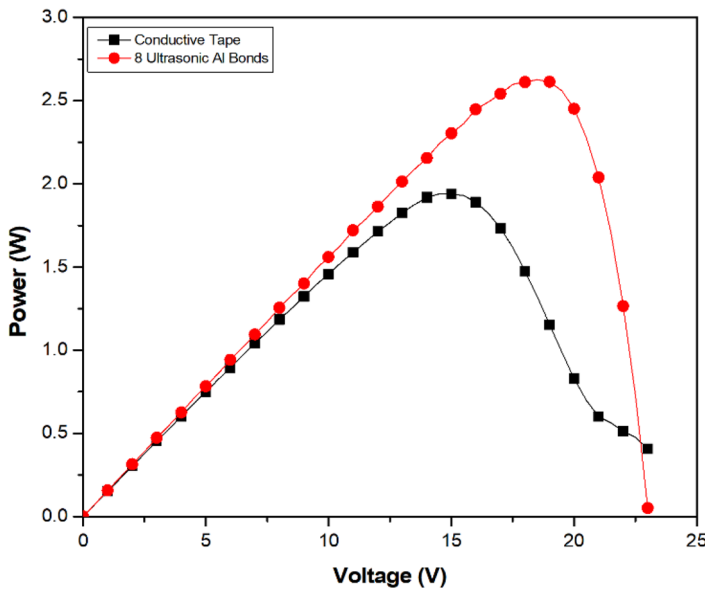


Figure 16. P-V curves of 8-bonds and conductive adhesive.

configuration. For the case of parallel connection, the dark line or hot spot area located at the gap between the two CIGS TFPV solar panels, as shown in Figure 14(c), can be used to further explains the occurrence of current leakages and abrupt changes of I_{sc} and P_{mpp} specifically for the after bonding and after bonding (on the busbar) connections. Hence, lock-in IR thermography can identify and explain the occurrence of defects that might affect the electrical performance of CIGS TFPV solar panels by identifying hot spot location and distribution.

Table 2. Electrical performance comparison between CIGS TFPV solar panels with 8-bonds configuration and conductive adhesive.

Configuration	V_{oc} (V)	I_{sc} (A)	J_{sc} (A/cm ²)	P_{mpp} (W)	FF (%)	Efficiency (%)
8 Bonds	22.56	0.16	0.00084	2.631	72.851	13.864
Conductive Adhesive	23.228	0.139	0.00076	1.92	59.09	10.464

The electrical performance evaluation of adhesive conductive tape was compared with the ultrasonic Al bond for the CIGS TFPV solar panel. It is because the adhesive conductive tape is the widely used interconnection in TFPV solar panels [33]. Figures 15 and 16 show the I-V and P-V curves of CIGS TFPV solar panels with 8-bonds configuration and conductive adhesive, respectively. Table 2 exhibits the electrical performance comparison between CIGS TFPV solar panels with 8-bonds configuration and conductive adhesive. Table 2 shows that the conductive adhesive has higher V_{oc} and lower I_{sc} , J_{sc} , P_{mpp} , FF, and efficiency values compared to the 8-bonds configuration. This indicates that conductive adhesive has lower bondability and efficiency than those 8-bonds. 32.49% efficiency improvement also shows that 8-bonds are the best-suited interconnection to be applied on CIGS TFPV solar panels.

4. Conclusion

Ultrasonic bonding and lamination have a big effect on how well CIGS TFPV solar panels with ultrasonic Al bonds work as electricity generators. It is shown that V_{oc} is the least affected electrical characteristic with the changes in connection of I-V measurement for each ultrasonic Al bonds configuration. The highest efficiency ranging from 11.45% to 13.86% for the 8-bonds configuration throughout unique connections of I-V measurement as compared to that of 16-bonds with an efficiency ranging from 7.99% to 10.77%, and parallel configurations, with an efficiency ranging from 9.14% to 11.92%, is because of the higher cumulative contact area of ultrasonic Al bonds and ribbons. The unique variation in the electrical characteristics of the 16-bonds configuration compared to that of the 8-bonds and parallel connection configurations is because of the presence of defects, namely short-circuited and shunted cells prior to the ultrasonic bonding. Further, the lowest efficiency of 11.82% for 16-bonds configuration, particularly after the lamination process, as compared to that of 8-bonds and parallel connection configurations, with efficiencies of 13.86% and 11.92%, respectively, is because of the minor cumulative contact area created between ultrasonic Al bonds and ribbon with Mo back contact layer. The abrupt increment of I_{sc} and P_{mpp} and the sudden decrement of J_{sc} and efficiency for the parallel configuration between after bonding and after bonding (on the busbar) connections are because of a gap along the edges of two CIGS TFPV solar panels. It has increased the possibility of current leakages happening prior to the lamination process. The increment in cumulative contact area that led to the increase in efficiency of the parallel configuration is because of the combined effects of thermal expansion, curing, and clamping forces that occurred during the lamination process. Physical inspection in terms of the shape of the ultrasonic bonds and ribbon, the location of the gap, and the occurrence of cracks on the glass substrate can explain the significant changes in electrical characteristics with the steps taken to produce

a laminated CIGS TPFV solar panel with the ultrasonic Al bonds. By figuring out where and how the hot spots are spread out, lock-in IR thermography can find and explain defects that might affect the electrical performance of CIGS TFPV solar panels. 32.49% efficiency improvement also shows that 8-bonds are the best-suited interconnection to be applied on CIGS TFPV solar panels.

Disclosure statement

No potential conflict of interest was reported by the author(s).

Funding

This work was sponsored by the Ministry of Higher Education of Malaysia under the Fundamental Research Grant Scheme [FRGS/1/2020/TKO/UNIKL/02/10] and Universiti Kuala Lumpur under Short Term Research Grant [str19087].

ORCID

Muhammad Nubli Zulkifli  <http://orcid.org/0000-0002-3293-3767>

References

- [1] Xu T, Valentini O, Luechinger C. Reliable metallic tape connection on CIGS solar cells by ultrasonic bonding. Paper presented at SPIE Solar Energy + Technology Conference. 2010 Aug 1–5; San Diego, CA, USA.
- [2] Heimann M, Klaerner P, Luechinger C, et al. Ultrasonic bonding of aluminum ribbons to interconnect high-efficiency crystalline-silicon solar cells. Energy Procedia. 2012;27:670–675. doi:[10.1016/j.egypro.2012.07.127](https://doi.org/10.1016/j.egypro.2012.07.127).
- [3] Ding Y, Kim J-K, Tong P. Effects of bonding force on contact pressure and frictional energy in wire bonding. Microelectron Reliab. 2006;46(7):1101–1112. doi:[10.1016/j.microrel.2005.09.010](https://doi.org/10.1016/j.microrel.2005.09.010).
- [4] Zhang G, Takahashi Y, Heng Z, et al. Ultrasonic weldability of al ribbon to cu sheet and the dissimilar joint formation mode. Mater. Trans. 2015;56(11):1842–1851. doi:[10.2320/matertrans.M2015251](https://doi.org/10.2320/matertrans.M2015251).
- [5] Ji H, Li M, Wang C, et al. In situ measurement of bond resistance varying with process parameters during ultrasonic wedge bonding. J Mater Process Technol. 2009;209(1):139–144. doi:[10.1016/j.jmatprotec.2008.01.036](https://doi.org/10.1016/j.jmatprotec.2008.01.036).
- [6] Tsanakas JA, Ha L, Buerhop C. Faults and infrared thermographic diagnosis in operating c-Si photovoltaic modules: a review of research and future challenges. Renew Sustain Energy Rev. 2016;62:695–709. doi:[10.1016/j.rser.2016.04.079](https://doi.org/10.1016/j.rser.2016.04.079).
- [7] Wehrmann A, Puttnins S, Hartmann L, et al. Analysis of laser scribes at CIGS thin-film solar cells by localized electrical and optical measurements. Opt Laser Technol. 2012;44(6):1753–1757. doi:[10.1016/j.optlastec.2012.01.009](https://doi.org/10.1016/j.optlastec.2012.01.009).
- [8] Misic B, Pieters BE, Schweitzer U, et al. Thermography and electroluminescence imaging of scribing failures in Cu(in,Ga)Se₂ thin film solar modules. Phys Status Solidi Appl Mater Sci. 2015;212(12):2877–2888. doi:[10.1002/pssa.201532322](https://doi.org/10.1002/pssa.201532322).
- [9] Basher H, Zulkifli MN, Rahmat MK, et al. Bondability of ultrasonic aluminum bonds on the molybdenum (de)selenide and molybdenum of back contact layer of copper indium gallium (de)selenide CIGS thin film photovoltaic solar panel. Sol Energy. 2021;228:516–522. doi:[10.1016/j.solener.2021.09.082](https://doi.org/10.1016/j.solener.2021.09.082).

- [10] Basher H, Zulkifli MN, Jalar A, et al. Temperature cycling test on ultrasonic aluminum bonds and conductive adhesive of copper indium gallium (di)selenide (CIGS) thin-film photovoltaic solar panel. *IEEE J. Photovoltaics.* 2022;12(6):1418–1427. doi:[10.1109/JPHOTOV.2022.3209021](https://doi.org/10.1109/JPHOTOV.2022.3209021).
- [11] Basher H, Zulkifli MN, Jalar A, et al. Effect of ultrasonic bonding parameters on the contact resistance and bondability performances of CIGS thin film photovoltaic solar panel. *IEEE J. Photovoltaics.* 2021;11(2):345–353. doi:[10.1109/JPHOTOV.2020.3047295](https://doi.org/10.1109/JPHOTOV.2020.3047295).
- [12] Vetter A, Fecher F, Adams J, et al. Lock-in thermography as a tool for quality control of photovoltaic modules. *Energy Sci Eng.* 2013;1(1):12–17. doi:[10.1002/ese3.1](https://doi.org/10.1002/ese3.1).
- [13] Adams J, Vetter A, Hoga F, et al. The influence of defects on the cellular open circuit voltage in CuInGaSe₂ thin film solar modules - An illuminated lock-in thermography study. *Sol Energy Mater Sol Cells.* 2014;123:159–165. doi:[10.1016/j.solmat.2014.01.014](https://doi.org/10.1016/j.solmat.2014.01.014).
- [14] Breitenstein O, Sturm S. Lock-in thermography for analyzing solar cells and failure analysis in other electronic components. *Quant Infrared Thermogr J.* 2019;16(3-4):203–217. doi:[10.1080/17686733.2018.1563349](https://doi.org/10.1080/17686733.2018.1563349).
- [15] Breitenstein O, Rakotoniaina JP, van der Heide ASHH, et al. Series resistance imaging in solar cells by lock-in thermography. *Prog Photovolt Res Appl.* 2005;13(8):645–660. doi:[10.1002/pip.623](https://doi.org/10.1002/pip.623).
- [16] Haque A, Bharath KVS, Khan MA, et al. Fault diagnosis of photovoltaic modules. *Energy Sci Eng.* 2019;7(3):622–644. doi:[10.1002/ese3.255](https://doi.org/10.1002/ese3.255).
- [17] Jordan DC, Silverman TJ, Sekulic B, et al. PV degradation curves: non-linearities and failure modes. *Progress in Photovoltaics.* 2017;25(7):583–591. doi:[10.1002/pip.2835](https://doi.org/10.1002/pip.2835).
- [18] de Amorim Soares G, Carolus J, Daenen M, et al. Round-robin of damp heat tests using CIGS solar cells. *Sol Energy.* 2021;214:393–399. doi:[10.1016/j.solener.2020.11.048](https://doi.org/10.1016/j.solener.2020.11.048).
- [19] van Deelen J, Frijters C. CIGS cells with metallized front contact: longer cells and higher efficiency. *Sol Energy [Internet].* 2017;143:93–99. doi:[10.1016/j.solener.2016.12.050](https://doi.org/10.1016/j.solener.2016.12.050).
- [20] Klasen N, Mondon A, Kraft A, et al. Shingled cell interconnection: a new generation of bifacial PV-Modules. Paper presented at 7th Workshop on Metallization & Interconnection for Crystalline Silicon Solar Cells. 2017 Oct 23–24; Constance, Germany.
- [21] Kim H, Wojkovich BG. Effects of mechanical damage and temperature on the electrical performance of CIGS thin-film solar cells. *IEEE J. Photovoltaics.* 2018;8(5):1331–1336. doi:[10.1109/JPHOTOV.2018.2858557](https://doi.org/10.1109/JPHOTOV.2018.2858557).
- [22] Salloom A, Abdulrazzaq O, Ismail B. Assessment of the performance of bifacial solar panels. *Int J Eng Tech Res.* 2018;8:13–17. https://www.erppublication.org/published_paper/IJETR2634.pdf.
- [23] Sharma V, Chandel SS. Performance and degradation analysis for long term reliability of solar photovoltaic systems: a review. *Renew Sustain Energy Rev.* 2013;27:753–767. doi:[10.1016/j.rser.2013.07.046](https://doi.org/10.1016/j.rser.2013.07.046).
- [24] Garcia PF, McLean RS, Hegedus S. Encapsulation of Cu(InGa)Se₂ solar cell with Al₂O₃ thin-film moisture barrier grown by atomic layer deposition. *Sol Energy Mater Sol Cells [Internet].* 2010;94(12):2375–2378. doi:[10.1016/j.solmat.2010.08.021](https://doi.org/10.1016/j.solmat.2010.08.021).
- [25] Sozzi G, Pignoloni D, Menozzi R, et al. Designing CIGS solar cells with front-side point contacts. In: 2015 IEEE 42nd Photovoltaic Specialist Conference (PVSC 2015). 2015. p. 8–12. New Orleans, LA, USA.
- [26] Spagnolo GS, Del Vecchio P, Makary G, et al. A review of IR thermography applied to PV systems. In: 2012 11th International Conference on Environment and Electrical Engineering EEEIC 2012 - Conference Proceedings. 2012. p. 879–884.
- [27] Kim D, Jang Y-JJ, Jung H-SS, et al. Optimization of CdS buffer layer for high efficiency CIGS solar cells. *j Nanosci Nanotechnol.* 2016;16(5):5074–5077. doi:[10.1166/jnn.2016.12171](https://doi.org/10.1166/jnn.2016.12171).
- [28] Reinhard P, Chirila A, Blosch P, et al. Review of progress toward 20% efficiency flexible CIGS solar cells and manufacturing issues of solar modules. *IEEE J. Photovoltaics.* 2013;3(1):572–580. doi:[10.1109/JPHOTOV.2012.2226869](https://doi.org/10.1109/JPHOTOV.2012.2226869).

- [29] Gerthoffer A, Roux F, Emieux F, et al. CIGS solar cells on flexible ultra-thin glass substrates: characterization and bending test. *Thin Solid Films*. 2015;592:99–104. doi:[10.1016/j.tsf.2015.09.006](https://doi.org/10.1016/j.tsf.2015.09.006).
- [30] Tippabhotla SK, Song WJR, Tay AAO, et al. Effect of encapsulants on the thermomechanical residual stress in the back-contact silicon solar cells of photovoltaic modules – a constrained local curvature model. *Sol Energy*. 2019;182:134–147. doi:[10.1016/j.solener.2019.02.028](https://doi.org/10.1016/j.solener.2019.02.028).
- [31] Song WJR, Tippabhotla SK, Tay AAO, et al. Effect of interconnect geometry on the evolution of stresses in a solar photovoltaic laminate during and after lamination. *Sol Energy Mater Sol Cells*. 2018;187:241–248. doi:[10.1016/j.solmat.2018.07.026](https://doi.org/10.1016/j.solmat.2018.07.026).
- [32] Eslami Majd A, Ekere NN. Crack initiation and growth in PV module interconnection. *Sol Energy*. 2020;206:499–507. doi:[10.1016/j.solener.2020.06.036](https://doi.org/10.1016/j.solener.2020.06.036).
- [33] Zarmai MT, Ekere NN, Oduoza CF, et al. A review of interconnection technologies for improved crystalline silicon solar cell photovoltaic module assembly. *Appl Energy*. 2015;154:173–182. doi:[10.1016/j.apenergy.2015.04.120](https://doi.org/10.1016/j.apenergy.2015.04.120).